23rd International Conference on Material Forming (ESAFORM 2020)

Microstructure and Properties of SLM AlSi10Mg: Understanding the Influence of the Local Thermal History

Anne Mertens[a]*, Jocelyn Delahaye[a], Olivier Dedry[a], Bénédicte Vertruyen[b], Jérôme T. Tchuindjang[a], Anne Marie Habraken[c]

[a]University of Liege, Faculty for Applied Science, Aerospace and Mechanics Department, Metallic Materials Science, Quartier Polytech 1, Allée de la Découverte, 13A, B-4000 Liège, Belgium
[b]University of Liege, Faculy of Sciences, LCIS - GreenMAT, Quartier Agora, Allée du 6 Août, 13, B-4000 Liège, Belgium
[c]University of Liège, Faculty for Applied Science, ArGEnCo Department, Materials and Solid Mechanics, Quartier Polytech 1, Allée de la Découverte, 13A, B-4000 Liège, Belgium

* Corresponding author. Tel.: +32 4 3669193; E-mail address: anne.mertens@uliege.be

Abstract

Selective Laser Melting (SLM) is an Additive Manufacturing technique that is widely used to produce AlSi10Mg parts with a good strength-to-weight ratio. Indeed, strongly refined microstructures are obtained due to the ultra-fast cooling rates reached in this process, conferring high strength to the parts, even in the as-built state. However, microstructural heterogeneities at the scale of the melt pool may exert a detrimental influence on the mechanical properties e.g. by causing a loss in ductility. This study thus aims at a better understanding of the influence of the local thermal history on local variations of microstructure and mechanical properties. Microscopy (i.e. SEM+EDS) and nanoindentation have been combined to reach a detailed knowledge of the local microstructure and properties. In particular, the solute Si content in the α-Al matrix, the volume fraction and the size of Si precipitates have been quantified by microscopy analysis. These local microstructural parameters are correlated with the matrix hardness as revealed by nanoindentation. Finally, the results of this detailed characterization are linked with the local thermal history that is approached in two different ways i.e. (i) an analytical description of thermal gradients inside the melt pool based on Rosenthal's and Matyja's equations and (ii) a simple Finite Element model for the deposition of a few layers in the SLM process.

1. Introduction

The powder-bed additive manufacturing process known as Selective Laser Melting (SLM) offers a great design flexibility, allowing for the fabrication of lattice structures [1], and of complex-shape structures whose design relies on topological optimization [2]. Moreover, SLM is known to impose extremely high cooling rates of 10^3-10^7 K/s during solidification giving rise to strongly refined structure and leading potentially to enhanced mechanical properties [3-5].

Aluminium alloys have long been extensively used e.g. in the transportation industry, in view of their many advantages such as their light weight, high specific strength and good corrosion resistance. Over the last few years, the processability of these alloys by additive manufacturing techniques - by SLM in particular - has received an ever increasing attention, and among the wide variety of Al alloys, the hypo-eutectic AlSi10Mg alloy has been the object of a strong focus due to its generally good castability and weldability, its high melt fluidity and low shrinkage upon solidification [4-6]. Nevertheless, some persistent issues keep limiting the use of SLM AlSi10Mg components as e.g. the presence of porosity or residual stresses in SLM Al parts [7]. Microstructural heterogeneities inherent to the layer-by-layer nature of additive

processes constitute a major challenge in that respect. Indeed, due to the difference of thermal histories between the core and the boundary of the melt pool, the microstructure of SLM AlSi10Mg parts is heterogeneous, exhibiting three distinct zones (Fig. 1) [8]:

- the core of the melt pool presents a structure of fine primary α-Al cells surrounded by an eutectic mixture of Al and Si precipitates (MP fine);
- the melt pool boundary is characterized by a coarser Al cellular/eutectic microstructure (MP coarse);
- moreover, on the outskirts of the melt pool, the intercellular eutectic network is partially broken by the coarsening of the Si phase. This latter zone was found to correspond to a MP fine zone of the previous layer which was affected by heat during the deposition of the new layer, similarly to the Heat Affected Zone in welding processes (HAZ) [9].
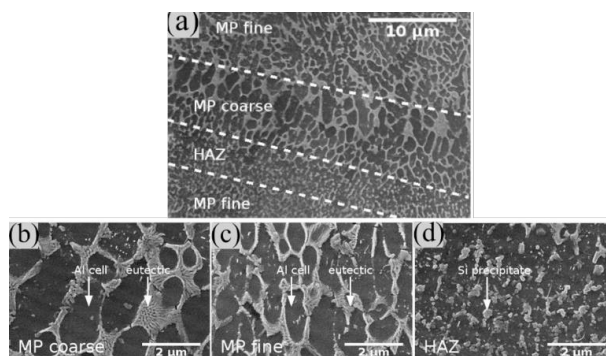

Fig. 1. (a) Microstructure at the melt pool boundary, (b) MP coarse, (c) MP fine, (d) HAZ.

This microstructural heterogeneity has been widely reported to play an important role in the fracture of SLM AlSi10Mg, although the exact mechanisms and location are still a matter of debate. Data from scientific literature present a large variability in that respect, reflecting on the large diversity of processing parameters and testing conditions (e.g. variation of the orientation of the loading direction with respect to the building direction in SLM) [10-21].

This study thus aims to present new data towards a better understanding of the influence of the local thermal history on local variations of microstructure and mechanical properties, following on our previous work [9] and on a recent study by Zhao et al. [7]. Microscopy (i.e. SEM+EDS) and nanoindentation have been combined to reach a detailed knowledge of the local microstructure and properties. Furthermore, the results of this detailed characterization are linked with the local thermal history assessed by two different methods i.e. (i) an analytical description of thermal gradients inside the melt pool and (ii) a simple Finite Element model for the deposition of a few layers in the SLM process.

2. Materials and methods

2.1. Samples fabrication

AlSi10Mg samples were fabricated in the vertical direction using a MTT SLM 250 machine with the following building parameters: a laser power of 175W, a scan speed of 195 mm/s, a powder layer thickness of 60 μm and a pre-heating temperature of 200°C for the building plate. As previously highlighted in [9], this choice of processing parameters enhances the thickness of the HAZ thus leading fracture to occur preferentially in this HAZ. Additional informations on samples production are also available in [22].

For comparison purposes, cylindrical samples of SLM AlSi10Mg material with a diameter of 5 mm and a thickness of 2 mm were re-heated above the melting temperature, and then re-solidified in a DTA NETZCH 449C Jupiter apparatus at a heating/cooling rate of 10K/min.

2.2. Microstructural characterization and nanoindentation

Samples for microscopy observation were polished following standard practices and etched with Keller's reagent i.e. 95 vol.% distilled water, 2.5 vol.% HNO_3, 1.5 vol.% HCl and 1 vol.% HF. Samples were observed by means of a SEM Philips XL30, and image analysis was carried out using the ImageJ software, in order to determine the Al cells size in the HAZ, MP coarse and MP fine zones. Moreover, the amount of Si in the HAZ, the MP coarse and the MP fine was determined by SEM+EDS analysis, combined with Monte Carlo EDS spectra simulations using the DTASII software to estimate more precisely the contribution of the Si precipitates to the signal. A more detailed description of these procedures may be found in [9].

The local hardness in the HAZ, the MP coarse and the MP fine was determined by nanoindentation using a Hysitron Ti950 Triboindenter with either a Berkovich or a cube corner tip. The penetration depth was set at 400 nm for indentation using the Berkovich tip, so as to measure the global hardness of each zone taking into account the contribution of both α-Al and Si phases. Alternatively, the cube corner tip was used to determine specifically the nano-hardness of the α-Al matrix, setting the penetration depth at 70 nm. The indentation zones are selected following in-situ Scanning Probe Imaging and controlled with SEM imaging.

2.3. Analytical model

In an attempt to better understand the effect of the processing parameters, the correlation between the typical size of the microstructure in the HAZ, MP coarse and MP fine, on the one hand, and the scan speed, the laser power and the pre-heating temperature, on the other hand, is evaluated by using Rosenthal's (Eq. (1)) [23] and Matyja's (Eq. (2)) [24] equations, as suggested by Tang et al. [25]. (Eq. (1)) provides the value of the temperature T. The parameters in (Eq. (1)) are defined as follow: x, y and z, the direction of the laser displacement, the direction transverse to the laser displacement and the building height direction,

respectively; v, the laser scan speed; t, the time; ξ, the moving coordinate system following the laser direction; P, the laser power; c, the absorbed power coefficient; k and α, the thermal conductivity and diffusivity of AlSi10Mg, respectively; T_0, T_{liq} and T_{sol}, the building plate temperature, the liquidus and solidus temperature of AlSi10Mg, respectively. The values of these parameters are summarized in Table 1 for this study, and for works from literature [7, 25]. The computed thermal field gives the location of the isolines of the solidus and liquidus. The interdistance between these lines depends on the melt pool depth. As the moving coordinates system relies on the time, both temperature and time variations are known. One can then compute the cooling rate $\dot{T}$ used in (Eq. (2)), giving in turn access to a calculated α-Al cell size following the method illustrated in our previous study (refer to Figure 2 in [9]). Once the model is validated by comparing the calculated and the experimental value of the cell size λ, it can be used to compute the thermal gradient controlling the thickness of the HAZ for the present study as well as for the works by Tang et al. [25] and Zhao et al. [7].

$$T = T_0 + \frac{Pc}{2\pi Rk} exp\left[\frac{-v(\xi+R)}{2\alpha}\right]$$

with

$$R = (\xi^2 + y^2 + z^2)$$

and

$$\xi = x - vt \tag{1}$$

$$\lambda = 43.2\dot{T}^{-0.324} \tag{2}$$

Table 1. Parameters used in Rosenthal's model for this work, and for studies by Tang et al. [25] and Zhao et al. [7]

Parameter	This study	Tang et al.	Zhao et al.
Conductivity, k [W/mK]	150	150	150
Diffusivity, α [m^2/s]	6.2 x 10^{-5}	6.2 x 10^{-5}	6.2 x 10^{-5}
Liquidus, T_{liq} [K]	867	867	867
Solidus, T_{sol} [K]	831	831	831
Building plate temperature, T_0 [K]	473	308	308
Laser Power , P [W]	175	370	390
Laser scan speed, v [m/s]	0.195	1.3	1.3
Absorbed power coefficient, c [-]	0.35	0.35	0.35

2.4. Finite Element model

Alternatively, the thermal history experienced by the AlSi10Mg parts has been investigated through a thermal finite element model of the SLM process. The temperature evolution in the part is given by the non-linear equation for an isotropic material

$$\nabla.k\nabla T + Q = \rho c_p \frac{\partial T}{\partial t} \tag{3}$$

where ∇ is the gradient operator; k is again the thermal conductivity, Q the power generated in the part, ρ the density, c_p the heat capacity and t the time. The enthalpy of fusion and vaporization are included in the heat capacity defining an apparent heat capacity.

The boundary condition at the free surface for the heat exchange is defined as

$$-k\nabla T.n = q_{laser} - h(T - T_{amb}) - \mathcal{E}\sigma(T^4 - T_{amb}^4) \tag{4}$$

where n is a unit vector normal to the surface; T_{amb}, the ambient temperature, h, the convection coefficient (taken as 20 W/m^{2}K); σ, the Stefan-Boltzmann's constant (5.67×10^{-8} W/m^{2}K^4), $\mathcal{E}$, the emissivity and q_{laser} the laser heat source. The laser is modeled by a Gaussian heat source:

$$q_{laser} = \frac{2AP}{\pi R^2} exp\left(\frac{2r^2}{R^2}\right) \tag{5}$$

where P is the laser power (set at 370 W); R, the laser beam radius (40 µm); A, the laser absorbed energy; r, the radial distance from the beam center.

Contrarily to the assumptions made for the analytical model that considered constant thermophysical properties (section 2.3), the thermophysical properties of the material are considered temperature dependent. For the base plate made of aluminium 2024, they are extracted from [26]. For the SLM AlSi10Mg, the properties have been determined experimentally in the MMS laboratory [27]. The thermophysical properties for the powder bed are estimated from the model of Sih and Barlow [28]. To switch between the unfused powder, no material and/or the bulk properties, element birth and death technique is employed. In the model, a fine mesh size is needed to capture the steep thermal gradient. This can lead to heavy computation costs. To limit those costs, 2D is used instead of 3D. Elements with 4 nodes are used with a size of 16 µm for the powder bed zone. The mesh of the system and boundary conditions are summarized in Fig. 2.
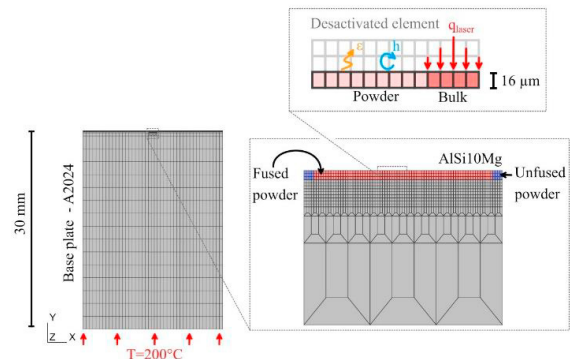

Fig. 2. Mesh of the A2024 base plate and the AlSi10Mg powder bed. The imposed temperature at the bottom of the base plate as well as heat loss by convection (ε) and radiation (h) at the top of the powder bed are represented. AlSi10Mg bulk elements are activated while powder elements are deactivated when the laser heat source q_{laser} moves across the powder bed.

3. Results and discussion

3.1. Identification of the preferred zone for failure

In our previous study on fracture mechanisms of SLM AlSi10Mg [9], samples were built vertically using a relatively low laser power of 175 W, a low laser scan speed of 0.195 m/s, a building plate temperature of 200°C (Table 1), with a powder layer thickness of 60 µm. In this case, fracture was found to occur preferentially in the HAZ on the basis of the following two observations:

- The dimple size on the fracture surface was found to match with the Si precipitate spacing in the MP fine and in the HAZ (Fig. 3). The Si precipitate spacing in the MP coarse, on the other hand, is inconsistent with the observed dimple size.
- The HAZ is found to be the weakest zone of the microstructure. Indeed, the HAZ exhibits a lower nano-hardness than the MP fine and MP coarse zones, as measured using a Berkovich tip and penetration depth of 400 nm (Fig. 4).
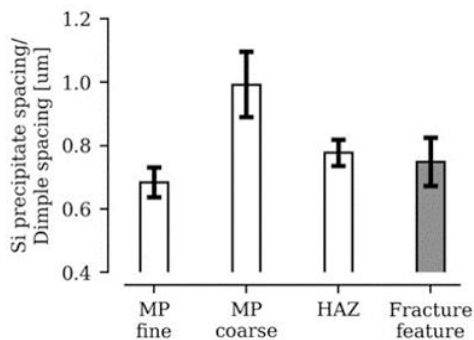

Fig. 3. Comparison of the Si precipitate spacing in each of the 3 zones of the microstructure (MP fine, MP coarse, HAZ) with the dimple spacing of the fracture surface of SLM AlSi10Mg tensile samples.

In the recent study by Zhao et al. [7], on the other hand, SLM AlSi10Mg samples were built horizontally with a higher laser power of 390W, a higher laser scan speed of 1.3 m/s, a relatively low building plate temperature of 35°C (Table 1) and a powder layer thickness of 30 µm. In this case, the HAZ is reported to barely contribute to damage. Instead, voids that formed on the interconnected Si-rich network are observed mainly in the melt pool interior, nearby the HAZ. Zhao et al. propose that this observation can be explained by the orientation of their samples i.e. because the loading direction (in the XY plane) is perpendicular to the building direction (Z) in the SLM process. This assumption deserves a deeper analysis.
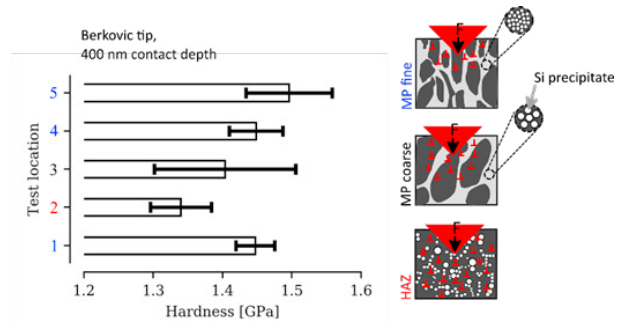

Fig. 4. Nano-hardness measured in the three different zones of the microstructure of SLM AlSi10Mg, using a Berkovich tip and under a penetration depth of 400 nm.

Indeed, the mechanical properties of SLM AlSi10Mg tensile specimens have sometimes been reported to greatly depend on their orientation on the building platform. More precisely, specimen with scan tracks oriented along the loading direction (XY) have been reported to exhibit higher tensile strength and/or ductility than the ones oriented perpendicularly (Z) [10, 29-31]. However, these effects have often been correlated with the significant presence of defects such as inter-layer porosities or spatters [10, 30]. Precise identification of the preferred zone for failure is often lacking, and when looking at the fracture surface, left hollow tunnels of the size of a scan track are observed also in XY-oriented specimen [14, 31]. Scan tracks parallel to the loading direction are pulled out leaving these hollow tunnels inside the material. Fracture thus appear to originate at the melt pool boundary, in the XY-oriented specimens as in Z-oriented samples, and sample orientation alone may not be sufficient to explain variations in fracture behaviour between different studies. It is our opinion that variations in the HAZ size as a result of different processing parameters should also be considered. This issue will be addressed in section 3.3, while section 3.2. focuses on analysing the strengthening mechanisms at play in the three different zones of the microstructures of SLM AlSi10Mg parts.

3.2. Strengthening mechanisms in the different zones of the microstructure.

Our previous study [9] has revealed that the amount of Si dissolved in the α-Al matrix exhibits small variations between the three zones of the microstructure of SLM, by using combined SEM+EDS analysis and Monte Carlo EDS spectra simulations with the DTASII software (Fig. 5). The three zones are found to differ from one another essentially by (i) the distribution of Si precipitates, in a network around small or coarse cells, and (ii) the size of the Si precipitates.
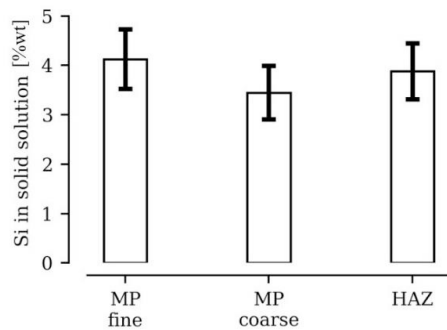
Fig. 5. Si in solid solution inside the MP fine, MP coarse and HAZ.

In order to help discriminate between the strengthening mechanisms of Si in solid solution of the Si precipitates, a reference specimen has been obtained by remelting a SLM AlSi10Mg sample and allowing the melt to solidify at a relatively slow cooling rate of 10 K/min using a DTA apparatus. Due to the slower cooling and solidification rates compared to those prevailing in SLM, the microstructure of the remelted sample is coarser and more homogeneous than the SLM microstructure. This makes it easier to analyse by SEM+EDS the local Si content dissolved in the α-Al matrix, as well as measuring the corresponding hardness by nano-indentation (using a cube corner tip and penetration depth of 70 nm) (Fig. 6). The local dissolved Si content and the local hardness present a good correlation, in agreement with [32].
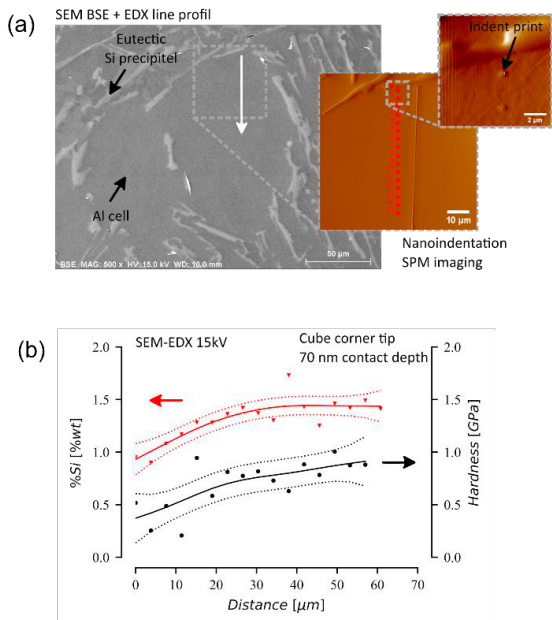

Fig. 6. (a) SEM Micrograph of the remelted AlSi10Mg reference sample, along with nano-indentation marks in SPM imaging; (b) graph showing the good correlation of the dissolved Si content and nano-hardness.

Based on the correlation validated on the remelted reference sample, it is then possible to link the dissolved Si content in the three different zones of SLM AlSi10Mg with the corresponding strengthening effect (Fig. 7). Solid solution strengthening is found to account for about 35% of the overall strengthening effect compared to pure Al, whereas Si precipitate appear as the dominant strengthening mechanism. Also note that the hardness values of Fig. 7 differ from the values of Fig. 4 due to the change of the testing condition. As a result of the smaller indent size for the measurements shown in Fig. 7, the contribution of the Si precipitate may actually be even under-estimated. X-ray diffraction and SEM+EBSD examinations are currently under progress with the hope of obtaining more precise estimate of dissolved Si content and of the local dislocation density, so as to refine this analysis.

Since the size and distribution of the Si precipitates - that are found to play an important role in strengthening the microstructure - are strongly influenced by the local thermal history experienced by SLM AlSi10Mg, the following section will address this issue in more details, by two different approaches i.e. (i) an analytical description of thermal gradients inside the melt pool based on Rosenthal's and Matyja's equations as described in section 2.3. and (ii) a simple Finite Element model for the deposition of a few layers in the SLM process (see section 2.4).
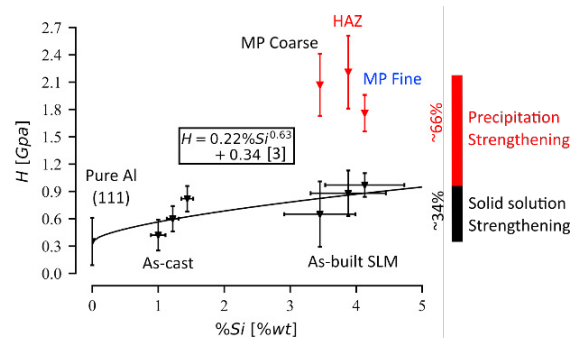

Fig. 7. Graph illustrating the respective contributions of solid solution strengthening and Si precipitate strengthening in the three zones of SLM AlSi10Mg. Nano-hardness measurements are carried out using a cube corner tip and under a penetration depth of 70 nm.

3.3. Correlating the microstructure with the thermal history

The size and distribution of Si precipitates in the three zones of the SLM AlSi10Mg microstructure, as well as the size of the HAZ, are strongly influenced by the local thermal history imposed by the choice of the processing parameters and the resulting heat input. A simple analytical model based on Rosenthal's equation (Eq. (1)) [23] and Matyja's equation (Eq. (2)) [24] (see section 2.3.) has been validated in [9] based on our own experimental observations and on the observations by Tang et al. [25]. In particular, variations in the HAZ thickness can be rationalized in correlation with the thermal gradient above the solidus, experienced locally at the melt pool boundary. To illustrate this relationship, Fig. 8 shows the curves of the thermal gradients as experienced at the bottom of

the melt pool, for the processing parameters of our previous study compared to the studies by Tang et al. [25] and Zhao et al. [7]. The processing parameters used by Zhao et al. [7] are expected to result in a steep temperature gradient, similar to the temperature gradient experienced in the study by Tang et al. [25], leading in turn to a thinner HAZ compared to our previous work [9]. This change in the HAZ thickness may thus also contribute to the difference in the preferred zone for failure, aside of the change in sample orientation.
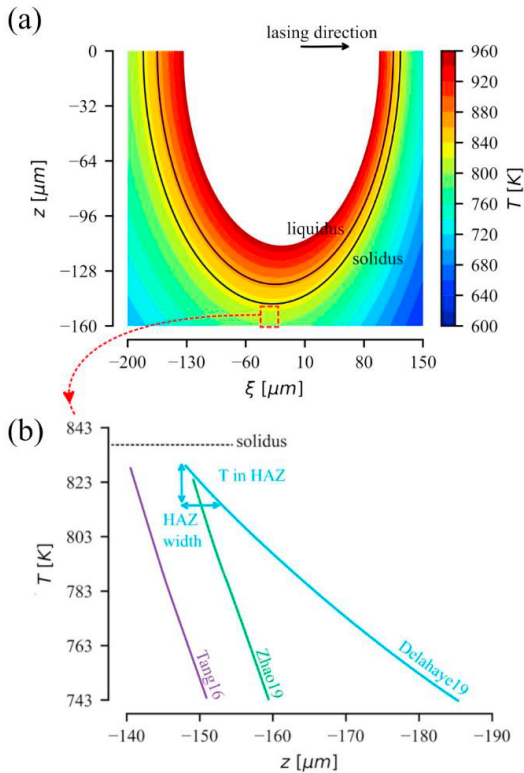

Fig. 8. (a) Melt pool profile obtained using's Rosenthal's equation and (b) Temperature profile at the bottom of the melt pool boundary.

Alternatively to this analytical model, a 2D FE thermal model has been developed for the deposition of the first few layers (section 2.4.). This thermal model is calibrated with our experimental data. The melt pool height has been determined through microscopy observations at a value of 110+/-10 μm, and the laser absorbed energy A has been tuned to a value of 0.02, so as to reach this size in the FEM model (Fig. 9(a)). Moreover, the cooling rate in the core of the melt pool is estimated at 10^6 K/s, based on the size of the microstructure and Matyja's empirical equation (Eq. (2)). The cooling rate given by the FE thermal model is 0.9×10^6 K/s (Fig. 9(b)), which is in very good agreement with the experimental value.

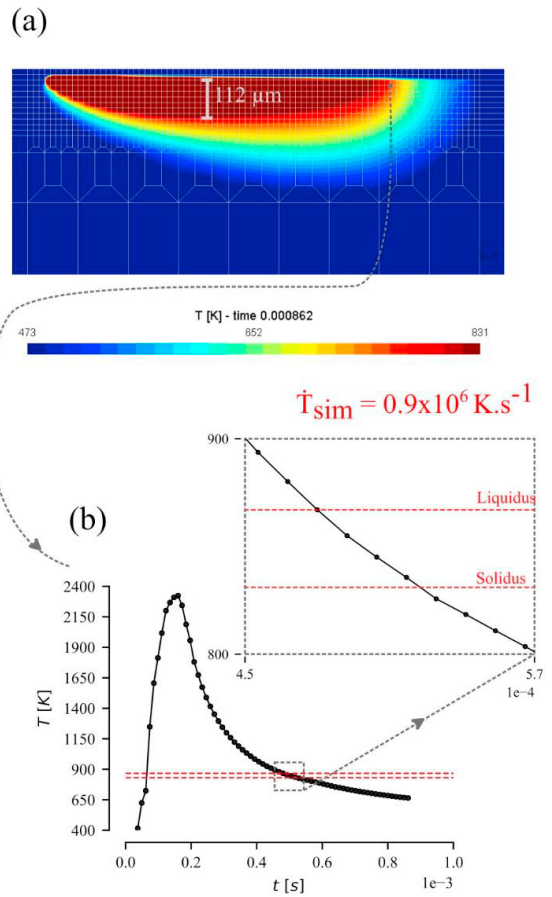Fig. 9. (a) Temperature map of the melt-pool after a steady state is reached at t=8.62x10-4s. The melt pool height is 112 μm. (b) Temperature with respect to the time for a node located in the core of the scan track. The cooling rate $\dot{T}_{sim}$ is calculated between the liquidus and the solidus temperatures.

The FE model allows to better take into account the properties of the considered materials, and all the processing parameters including also the layer thickness that is neglected in the analytical model. Yet, in spite of its somewhat simplistic underlaying assumptions as considering constant thermophysical properties or completely neglecting some processing parameters as the powder layer thickness, hatch spacing…, the analytical model proves a simple and efficient tool when it comes to the sole purpose of rationalizing the effect of the processing parameters on the HAZ size.

4. Conclusions

This study thus aims to bring new insights and contribute towards a better understanding of the influence of the local thermal history on local variations of microstructure and mechanical properties in SLM AlSi10Mg. A particular attention is thus given to microstructural heterogeneities that may play a detrimental role in fracture mechanisms.

Based on detailed microscopy (i.e. SEM+EDS) and nanoindentation analysis, precipitate strengthening is identified

as the dominant strengthening mechanism, compared to the lower contribution of solid solution strengthening by Si dissolved in the α-Al matrix.

Since the size and distribution of the Si precipitates are strongly influenced by the local thermal history experienced by SLM AlSi10Mg, two different approaches were attempted in order to correlate these microstructural features with the local thermal history i.e. (i) an analytical description of thermal gradients inside the melt pool and (ii) a simple 2D FE model for the deposition of a few layers in the SLM process. The FE model allows to take accurately into account all the main processing parameters including also those neglected in the analytical model, and to consider temperature-dependent thermophysical properties of the considered materials. Yet, in spite of its somewhat simplistic underlaying assumptions (e.g. considering constant thermophysical properties…), the analytical model proves a simple and very efficient tool to help rationalizing the effect of the processing parameters on the HAZ size.

Acknowledgements

References

[1] Qiu C, Yue S, Adkins NJE, Ward M, Hassanin H, Lee PD, Withers PJ, Attallah MM, Influence of processing conditions on strut structure and compressive properties of cellular lattice structures fabricated by selective laser melting, Mater Sci Eng A 2015; 628:188–197.
[2] Li Z, Zhang DZ, Dong P, Kucukkoc I. A lightweight and support-free design method for selective laser melting. Int J Adv Manuf Technol 2017; 90:2943-2953.
[3] Kimura T, Nakamoto T, Microstructures and mechanical properties of A356 (AlSi7Mg0.3) aluminum alloy fabricated by selective laser melting, Mater Des 2016; 89:1294–1301.
[4] Mertens AI, Delahaye J, Lecomte-Beckers J, Fusion-based additive manufacturing for processing aluminium alloys : state-of-the-art and challenges, Adv Eng Mater 2017; 19:1700003.
[5] Trevisan F, Calignano F, Lorusso M, Pakkanen J, Aversa A, Ambrosio EP, Lombardi M, Fino P, Manfredi D, On the selective laser melting (SLM) of the AlSi10Mg alloy: process, microstructure, and mechanical properties, Materials 2017; 10:76
[6] Brandl E, Heckenberger U, Holzinger V, Buchbinder D, Additive manufactured AlSi10Mg samples using Selective Laser Melting (SLM): Microstructure high cycle fatigue and fracture behaviour, Mater Des 2012; 34:159-169.
[7] Zhao L, Santos Macias JG, Ding L, Idrissi H, Simar A, Damage mechanisms in selective laser melted AlSi10Mg under as built and different post-treatment conditions, Mater Sci Eng A 2019; 764:138210
[8] Thijs L, Kempen K, Kruth JP, Van Humbeeck J, Fine-structured aluminium products with controllable texture by selective laser melting of pre-alloyed AlSi10Mg powder, Acta Mater 2013; 61:1809–1819.

[9] Delahaye J, Tchuindjang JT, Lecomte-Beckers J, Habraken AM, Mertens A, Influence of Si precipitates on fracture mechanisms of AlSi10Mg parts processed by Selective Laser Melting, Acta Mater 2019; 175:160-170.
[10] Tang M, Pistorius PC, Anisotropic Mechanical Behavior of AlSi10Mg Parts Produced by Selective Laser Melting, JOM 2017; 69:516–522.
[11] Aboulkhair NT, Maskery I, Tuck C, Ashcroft I, Everitt NM, Improving the fatigue behaviour of a selectively laser melted aluminium alloy: Influence of heat treatment and surface quality, Mater. Des. 2016; 104:174–182.
[12] Suryawanshi J, Prashanth KG, Scudino S, Eckert J, Prakash O, Ramamurty U, Simultaneous enhancements of strength and toughness in an Al-12Si alloy synthesized using selective laser melting, Acta Mater 2016; 115:285–294.
[13] Prashanth KG, Scudino S, Klauss HJ, Surreddi KB, Löber L, Wang Z, Chaubey AK, Kühn U, Eckert J, Microstructure and mechanical properties of Al–12Si produced by selective laser melting: Effect of heat treatment, Mater. Sci. Eng. A. 2014; 590:153–160.
[14] Rosenthal I, Stern A, Frage N, Strain rate sensitivity and fracture mechanism of AlSi10Mg parts produced by Selective Laser Melting, Mater Sci Eng A 2017; 682:509–517.
[15] Takata N, Kodaira H, Sekizawa K, Suzuki A, Kobashi M, Change in microstructure of selectively laser melted AlSi10Mg alloy with heat treatments, Mater Sci Eng A 2017; 704:218–228.
[16] Siddique S, Imran M, Walther F, Very high cycle fatigue and fatigue crack propagation behavior of selective laser melted AlSi12 alloy, Int J Fatigue 2017; 94:246–254.
[17] Rao H, Giet S, Yang K, Wu X, Davies CHJ, The influence of processing parameters on aluminium alloy A357 manufactured by Selective Laser Melting, Mater Des 2016; 109:334–346.
[18] Kim DK, Woo W, Hwang JH, An K, Choi SH, Stress partitioning behavior of an AlSi10Mg alloy produced by selective laser melting during tensile deformation using in situ neutron diffraction, J Alloys Compd 2016; 686:281–286.
[19] Wei P, Wei Z, Chen Z, Du J, He Y, Li J, Zhou Y, The AlSi10Mg samples produced by selective laser melting: single track, densification, microstructure and mechanical behavior, Appl Surf Sci 2017; 408: 38–50.
[20] Li W, Li S, Liu J, Zhang A, Zhou Y, Wei Q, Yan C, Shi Y, Effect of heat treatment on AlSi10Mg alloy fabricated by selective laser melting: Microstructure evolution, mechanical properties and fracture mechanism, Mater Sci Eng A 2016; 663:116–125.
[21] Pfaff A, Jäcklein M, Hoschke K, Wickert M, Designed Materials by Additive Manufacturing—Impact of Exposure Strategies and Parameters on Material Characteristics of AlSi10Mg Processed by Laser Beam Melting, Metals. 2018; 8:491.
[22] Mertens A, Dedry O, Reuter D, Rigo O, Lecomte-Beckers J, Thermal Treatments of AlSi10Mg Processed by Laser Beam Melting, Proc. 26th Int. Solid Free Fabr Symp, Austin, 2015; 1007–1016.
[23] Rosenthal D, Mathematical theory of heat distribution during welding and cutting, Weld J 1941; 20:220–234.
[24] Matyja H, The Effect of Cooling Rate on the Dendrite Spacing in Splat-Cooled Aluminium Alloys, J Inst Met 1968; 96:30–32.
[25] Tang M, Pistorius PC, Narra S, Beuth JL, Rapid Solidification: Selective Laser Melting of AlSi10Mg, JOM 2016; 68: 960–966.
[26] Mills KC, Recommended values of thermophysical properties for selected commercial alloys, Cambridge: Woodhead; 2002.
[27] Delahaye J, Thermophysical properties of AlSi10Mg SLM, Internal report, University of Liège - MMS Laboratory, 2018.
[28] Sih SS, Barlow JW, The Prediction of the Emissivity and Thermal Conductivity of Powder Beds, Part Sci Technol 2004; 22:427–440.
[29] Hitzler L, Janousch C, Schanz J, Merkel M, Heine B, Mack F, Hall W, Öchsner A, Direction and location dependency of selective laser melted AlSi10Mg specimens, J Mater Process Technol 2017; 243:48–61.
[30] Anwar AB, Pham QC, Selective laser melting of AlSi10Mg: Effects of scan direction, part placement and inert gas flow velocity on tensile strength, J Mater Process Technol 2017; 240:388-396.
[31] Ch SR, Raja A, Nadig P, Jayaganthan R, Vasa NJ, Influence of working environment and built orientation on the tensile properties of selective laser melted AlSi10Mg alloy, Mater Sci Eng A 2019; 750:141-151.
[32] E. Sjölander, Seifeddine S, Svensson IL, Modelling yield strength of heat treated Al–Si–Mg casting alloys, Int J Cast Metal Res 2011; 24:338-345.